Quantum states and interband optical spectra in spherical GaAs-(Ga,Al)As quantum dots doped with on-centre shallow donor impurities: a real-time wavepacket propagation method

2000 J. Phys.: Condens. Matter 12 9917

(http://iopscience.iop.org/0953-8984/12/48/308)

J. Phys.: Condens. Matter **12** (2000) 9917–9932. Printed in the UK PII: S0953-8984(00)13823-8

Quantum states and interband optical spectra in spherical GaAs-(Ga,Al)As quantum dots doped with on-centre shallow donor impurities: a real-time wavepacket propagation method

Diego F Montaño†, Julio C Arce† and Nelson Porras-Montenegro‡§

† Departamento de Química, Universidad del Valle, A.A. 25360, Cali, Colombia

‡ Departamento de Física, Universidad del Valle, A.A. 25360, Cali, Colombia

Received 9 May 2000, in final form 21 September 2000

Abstract. A time-dependent approach for the calculation of eigenenergies, eigenfunctions and optical spectra, within the effective-mass and single-hole-band approximations, of low-dimensional semiconductor systems is presented. In this method, energy and optical spectra are obtained by Fourier analysis of a time-autocorrelation function constructed from an appropriately chosen propagated wavepacket. Eigenfunctions are determined by a direct Fourier analysis of such a propagated wavepacket. The time evolution of the wavefunction is obtained by numerical integration of the time-dependent Schrödinger equation. This approach shares the virtues of the more common numerical methods (accuracy, flexibility and automatic enforcement of boundary conditions) with the additional advantage that it can yield an entire eigen or optical spectrum in a single calculation. The methodology is applied to the calculation of all the eigenenergies and eigenfunctions of the conduction band, and the intensities of the transitions from the ground state of the valence band to all the states of the conduction band, in spherical GaAs-(Ga,Al)As quantum dots with finite confinement and a wide range of radii, without and with an on-centre shallow donor impurity.

1. Introduction

With the development of experimental techniques such as chemical vapour deposition, liquid-phase epitaxy and molecular-beam epitaxy, it has been possible in the last two decades, to fabricate a variety of low-dimensional semiconductor systems with sizes comparable to the electronic de Broglie wavelength [1]. Such systems include quantum dots (QD's), quantum-well wires (QWW's) and single and multiple quantum wells (QW's), in which carriers are free to move in zero, one and two dimensions, respectively. Due to carrier confinement, these structures exhibit electronic, optical and transport properties that are quite different from those of the semiconductor constituents. In the past few years, a large number of experimental [2] and theoretical [3–7] studies of the electronic structure, impurity and excitonic states, intraband and interband optical spectra, and transport phenomena in such low-dimensional semiconductor systems have been reported.

The dependence of these properties on the size of the system, the position of the impurity in the structure and the strength and direction of applied electric and magnetic fields is of special interest. Extensive theoretical investigations of such dependences require large amounts of calculations, which can become very time-consuming and tedious. Therefore, it is

§ Corresponding author.

0953-8984/00/489917+16$30.00

desirable to implement computational methodologies that are, besides accurate, also flexible, efficient and accessible to the experimentalist as well as to the theoretician. A variety of computational approaches have been used, such as approximate perturbative, variational and basis-set methods [4] on the one hand and exact numerical techniques in real [5, 6] or momentum [7] space on the other hand. In variational or basis-set approaches, the quality of the solutions depends strongly on the chosen trial function or basis set, which may work well for a certain regime of length and/or energy scales, but may fail for another regime, precluding a treatment of the different regimes on a common footing. In addition, in variational methods only one solution is obtained at a time, whereas in basis-set techniques only a few (usually the lowest) eigensolutions have physical significance, sometimes their very identification being difficult. Numerical approaches for the direct integration of the time-independent Schrödinger equation (TISE) [5–7] yield exact solutions, in the sense that no intrinsic approximations are entailed and the error is purely numerical and controlled. They are also very flexible, since they can deal with potentials of arbitrary shape, and are easily accessible [8]. However, they still yield only one solution at a time.

An interesting alternative to time-independent numerical methods is offered by wavepacket propagation methods [9–12], which rely on the direct numerical integration of the *time-dependent* Schrödinger equation (TDSE). It may seem awkward to employ an approach that involves solving the TDSE for finding solutions of the TISE, but this can be advantageous. In particular, in time-dependent methods the boundary conditions are enforced automatically, since the TDSE is an initial-value problem, in contrast to time-independent methods where the boundary conditions must be adjusted during the calculation, since the TISE is a boundary-value problem [6]. Kuhn *et al* [9] have employed a relaxation approach for the calculation of eigenenergies and eigenfunctions within the effective-mass approximation (EMA) [3]. In this method, a wavepacket is propagated numerically in *imaginary* time until it converges, within a normalization constant, to the ground state. For obtaining an excited state this procedure must be repeated employing an initial wavepacket orthogonal to the already calculated lower states.

Recently, methods based on the propagation of wavepackets in *real* time have become popular in atomic and molecular physics [10–12]. In these methods, the computation of eigenenergies involves the construction of a so-called time-autocorrelation function from an appropriate nonstationary solution of the TDSE, whose Fourier transform displays the energies of all the stationary states comprised in such a nonstationary wave function [10]. Eigenfunctions are computed from a direct Fourier transform of the time-dependent wave function at the corresponding eigenenergies [10, 11]. A related procedure for calculating densities of states in solids, based on the Fourier analysis of the retarded Green function has also been presented [13]. Photoabsorption and Raman scattering spectra can also be computed directly by Fourier analysis of so-called dipole correlation functions [11, 12], analogously to the manner it is done in condensed-phase spectroscopy [14]. These approaches share the virtues (accuracy, flexibility and automatic enforcement of boundary conditions) of the previously mentioned numerical methods, with the additional advantage that they can yield an entire eigen or optical spectrum *in a single calculation*. This last feature makes this approach very suitable for investigations that require the determination of many eigen and/or optical spectra.

The first objective of this work is to show how a numerical real-time wavepacket propagation method (RTWPM) can be adapted and implemented for the calculation, within the EMA and the single-hole-band approximation, of the quantum states and optical spectra of low-dimensional semiconductors. The second objective is to apply the RTWPM to an extensive and systematic study of all the bound quantum states of the conduction band and of the optical spectra associated with transitions from the ground state of the valence band to all the bound states of the condition band, in spherical GaAs-(Ga,Al)As QD's with finite

confinement and a wide range of radii, without and with an on-centre shallow donor impurity. The impurity-free finite spherical well is a standard textbook example, having analytical solutions in the form of a transcendental equation involving spherical Bessel functions. (In practice, however, such a transcendental equation is commonly solved iteratively [15].) The impurity-doped finite spherical well, on the other hand, has been treated by means of a variational approach [15]. These systems have been chosen for the following reasons. First, to date there are no experimental reports on the optical spectra associated with interband transitions in them, although their understanding might become relevant in solid-state physics and technology, particularly in the field of optoelectronics. Second, a theoretical study of these spectra, including *all* the allowed transitions, has not been provided either.

In section 2, the model employed for the spherical QD is set up. Section 3 presents the general formalism of the RTWPM for the calculation of energy eigenvalues, eigenfunctions and intensities of optical transitions, together with its adaptation for the model of section 2. In section 4, the computational strategies chosen for the efficient implementation of the RTWPM are summarized. In section 5, the results of the calculations are displayed and discussed. Section 6 closes with the concluding remarks.

2. Model

In this work, the EMA [3, 15] and the single-hole-band approximation [3, 15] (in which the hole effective mass is taken as an appropriate average of the light-hole and heavy-hole effective masses) are taken as a starting point. Additionally, for the sake of simplicity, the electron–hole interaction is not taken into account, i.e. excitonic effects [3] are not considered, the dielectric constant and effective masses are considered equal for the GaAs and (Ga,Al)As materials [15], the dielectric constant is taken as position-independent [15] and the effective masses are taken as isotropic [3, 15].

Accordingly, the (radial) confinement potentials for the electron and hole in a spherical QD of radius R, $V_{\mathrm{conf}}^{(\mathrm{e,h})}(r)$, are modelled as step functions of height $V_0^{(\mathrm{e,h})}$ at R, and the electron–impurity interaction, $V_{\mathrm{imp}}(r)$, is taken as pure Coulombic. The wave function for the electron (hole) is written as [3]

$$\Theta_{k_0,s}^{(\mathrm{e,h})}(\vec{r}) = U_{k_0,s}^{(\mathrm{e,h})}(\vec{r})\xi^{(\mathrm{e,h})}(\vec{r}) \tag{1}$$

where $U_{k_0,s}^{(\mathrm{e,h})}(\vec{r})$ is the periodic Bloch function evaluated as the sth band extreme, k_0, and $\xi^{(\mathrm{e,h})}(\vec{r})$ is the envelope eigenfunction, which can be separated in the standard form [16]

$$\xi_{n,l,m}^{(\mathrm{e,h})}(r,\theta,\phi) = \frac{1}{r}\psi_{n,l}^{(\mathrm{e,h})}(r)Y_{l,m}(\theta,\phi) \tag{2}$$

with $Y_{l,m}(\theta,\phi)$ a spherical harmonic and $\psi_{n,l}^{(\mathrm{e,h})}(r)$ a radial eigenfunction. With this form, the latter satisfies the boundary condition $\psi_{n,l}^{(\mathrm{e,h})}(r=0)=0$ and is an eigensolution of the l-wave radial TISE

$$\hat{H}_l^{(\mathrm{e,h})}\psi_{n,l}^{(\mathrm{e,h})}(r) = E_{n,l}^{(\mathrm{e,h})}\psi_{n,l}^{(\mathrm{e,h})}(r) \tag{3}$$

with the radial Hamiltonian

$$\hat{H}_l^{(\mathrm{e,h})} = -\frac{\hbar^2}{2m_{\mathrm{e,h}}^*}\frac{\partial^2}{\partial r^2} + V_l^{(\mathrm{e,h})}(r). \tag{4a}$$

Here,

$$V_l^{(\mathrm{e,h})}(r) = \frac{\hbar^2 l(l+1)}{2m_{\mathrm{e,h}}^* r^2} + V^{(\mathrm{e,h})}(r) \tag{4b}$$

is the familiar effective radial potential for the electron (hole) of effective mass $m^*_{e,h}$, with $V^{(e)}(r) = V^{(e)}_{conf} + V_{imp}$ for the electron and $V^{(h)}(r) = V^{(h)}_{conf}$ for the hole.

Within the EMA, the intensity of an optical transition from an initial state $\Theta_{k_0,s}(\vec{r})$ to a final state $\Theta_{k_0,s'}(\vec{r})$ is given by [17]

$$I \propto |\langle \Theta_{k_0,s}(\vec{r})|\vec{\varepsilon}\cdot\hat{\vec{p}}|\Theta_{k_0,s'}(\vec{r})\rangle|^2 \tag{5}$$

where $\vec{\varepsilon}$ is the polarization vector of the applied electromagnetic field and $\hat{\vec{p}}$ is the momentum operator. For an interband transition this intensity can be further approximated as [17]

$$\begin{aligned} I &\propto |\vec{K}_{s,s'}\cdot\langle \xi_{n,l,m}(r,\theta,\phi)|\vec{\varepsilon}|\xi_{n',l',m'}(r,\theta,\phi)\rangle|^2 \\ &= |\vec{K}_{s,s'}\cdot\langle Y_{l,m}(\theta,\phi)|\vec{\varepsilon}|Y_{l',m'}(\theta,\phi)\rangle|^2 \left|\left\langle \psi_{n,l}(r)\left|\frac{1}{r^2}\right|\psi_{n',l'}(r)\right\rangle\right|^2 \end{aligned} \tag{6}$$

where $\vec{K}_{s,s'} \equiv \langle U_{k_0,s}(\vec{r})|\hat{\vec{p}}|U_{k_0,s'}(\vec{r})\rangle$, and equation (2) has been used. The first factor of equation (6) gives rise to the well known $E1$ selection rules [16, 17]

$$\Delta l = l' - l = \pm 1 \tag{7a}$$

$$\Delta m = m' - m = 0, \pm 1 \tag{7b}$$

whereas the second factor determines the relative transition intensities.

3. Formalism of the RTWPM

For the determination of the eigenenergies and eigenfunctions of a Hamiltonian, the first step consists of the specification of a *test function*, whose spatial form corresponds to a wavepacket. This function must satisfy the boundary conditions of the problem, otherwise being arbitrary at this point. The test function can be written formally as a spectral expansion in terms of the eigenstates of the Hamiltonian,

$$\Psi(\vec{r}) = \sum_j c_j \psi_j(\vec{r}) \tag{8}$$

where j denotes the complete set of relevant quantum numbers. Here and below, for the sake of notational simplicity, the summation symbol is understood to include the integration over the continuous part of the spectrum. The second step entails the propagation in time of the test function, assuming, merely for convenience, the initial time as $t = 0$. The formal spectral expansion now takes the form

$$\Psi(\vec{r},t) = \sum_j c_j \psi_j(\vec{r}) \exp(-\iota E_j t/\hbar). \tag{9}$$

Since, in practice, it is impossible to generate the wave function for $-\infty < t < \infty$, from now on a record of time $-T \leqslant t \leqslant +T$ will be assumed.

For the determination of eigenenergies, the next step consists in constructing a *time-autocorrelation function*, which is defined as the spatial overlap of the test function at $t = 0$ with itself at t:

$$A(t) := \langle \Psi|\Psi(t)\rangle \tag{10}$$

$$= \sum_j |c_j|^2 \exp(-\iota E_j t/\hbar) \tag{11}$$

where, to obtain the last equation, equation (9) has been employed. The formal spectral representation (11) shows that $A(t)$ contains information about the spectral weights, $|c_j|^2$, and

energies, E_j, of the stationary states comprised in the test function. Finally, a *spectral function* is evaluated, which is defined as the truncated inverse Fourier transform of $A(t)$:

$$\Omega_T(E) := \frac{1}{2\pi\hbar}\int_{-T}^{T} A(t)\exp(\imath Et/\hbar)\,\mathrm{d}t \tag{12}$$

$$= \sum_j |c_j|^2 \delta_T(E - E_j) \tag{13}$$

where, to obtain the last equation, equation (11) has been employed and a normalized lineshape function

$$\delta_T(E) := \frac{1}{2\pi\hbar}\int_{-T}^{T} \exp(\imath Et/\hbar) \tag{14}$$

$$= \frac{\sin(ET/\hbar)}{\pi E} \tag{15}$$

has been introduced. In the limit of $T \to \infty$ this is the familiar Fourier representation of the Dirac delta function, $\lim_{T\to\infty}\delta_T(E) = \delta(E)$. For finite T, this oscillatory function presents a global maximum at $E = 0$ of height $T/\pi\hbar$ and nodes at $E = \pm k\pi\hbar/T$, with $k = 1, 2, \ldots$. Thus, for sufficiently long T, the function looks like a peak of breadth $\Delta E \sim 2\pi\hbar/T$. Consequently, for long enough T, in the *discrete* part of the spectrum the spectral function consists of a series of peaks centred at the eigenenergies of the Hamiltonian. A peak located at E_j will be well resolved (i.e. approximately orthogonal to the other peaks) if $\Delta E \ll |E_{j+1} - E_{j-1}|$, that is, if $T \gg 2\pi\hbar|E_{j+1} - E_{j-1}|^{-1}$, its height, $\Omega_T(E_j)$, giving the corresponding spectral weight by

$$|c_j|^2 \approx \frac{\pi\hbar}{T}\Omega_T(E_j) \tag{16}$$

where $\delta_T(0) = T/\pi\hbar$ has been used. Therefore, in accordance with the time-energy uncertainty principle, the longer the propagation time the greater the resolution of the obtained discrete eigenstates.

The eigenfunctions can be obtained by means of the *spectral surface*, which is defined as the truncated inverse Fourier transform to the energy domain of the time-propagated test function:

$$\Sigma_T(\vec{r}, E) := \frac{1}{2\pi\hbar}\int_{-T}^{T} \Psi(\vec{r}, t)\exp(\imath Et/\hbar)\,\mathrm{d}t \tag{17}$$

$$= \sum_j c_j\psi_j(\vec{r})\delta_T(E - E_j) \tag{18}$$

where, to obtain the last equation, equations (9) and (14) have been employed. It is observed that, for sufficiently long T, a 'slice' of the spectral surface at the *discrete* eigenvalue $E = E_j$, produces the corresponding normalized eigenfunction by

$$\psi_j(\vec{r}) \approx \frac{\pi\hbar}{Tc_j}\Sigma_T(\vec{r}, E_j). \tag{19}$$

Once the eigenfunctions are obtained, transition intensities can be determined in the usual manner, by computing the matrix elements of the relevant interaction operator between the initial and the final states. However, the RTWPM provides a strategy for obtaining an entire optical spectrum in a single calculation from the eigenfunction of the initial state only. The formalism differs from the one for determining eigenenergies solely by the test function employed. In the special case of an interband spectrum, an *optical* ($E1$) *test function* is

prescribed by

$$\Psi^{(E1)}(\vec{r}) \equiv \psi_0(\vec{r}) \tag{20}$$

$$= \sum_j \langle \psi_j | \psi_0 \rangle \psi_j(\vec{r}) \tag{21}$$

where $\psi_0(\vec{r})$ is the (known) eigenfunction of the initial state and closure has been introduced in order to obtain the last equation. It is seen that the coefficients appearing in this spectral expansion are precisely the matrix elements governing the intensity of the optical interband transition, as indicated by equation (6). Next, the $E1$ test function is propagated in time, and an $E1$ time-autocorrelation function is constructed as

$$A^{(E1)}(t) := \langle \Psi^{(E1)} | \Psi^{(E1)}(t) \rangle \tag{22}$$

$$= \sum_j |\langle \psi_j | \psi_0 \rangle|^2 \exp(-\imath E_j t/\hbar). \tag{23}$$

Finally, an $E1$ spectral function is obtained by

$$\Omega_T^{(E1)}(E) := \frac{1}{2\pi\hbar} \int_{-T}^{T} A^{(E1)}(t) \exp(\imath E t/\hbar)\, \mathrm{d}t \tag{24}$$

$$= \sum_j |\langle \psi_j | \psi_0 \rangle|^2 \delta_T(E - E_j). \tag{25}$$

It is observed that, for $T \gg 2\pi\hbar |E_{J+1} - E_{j-1}|^{-1}$, in the *discrete* part of the spectrum this function presents resolved peaks centred at the eigenenergies, whose heights, $\Omega_T^{(E1)}(E_j)$, are proportional to the transition intensities of the corresponding transitions:

$$|\langle \psi_j | \psi_0 \rangle|^2 \approx \frac{\pi\hbar}{T} \Omega_T^{(E1)}(E_j). \tag{26}$$

The formalism just presented is entirely general in the sense that the nature of the Hamiltonian has remained unspecified. Its adaptation to the problem posed in section 2 is easily achieved in the following fashion. For the determination of l-wave eigenenergies and eigenfunctions, an l-wave radial test function is chosen according to the criteria explained in section 5. Analogously to equation (8), this function can be formally expressed as

$$\Psi_l^{(\mathrm{e,h})}(r) = \sum_n c_{n,l}^{(\mathrm{e,h})} \psi_{n,l}^{(\mathrm{e,h})}(r). \tag{27}$$

This test function is then propagated in time with the corresponding l-wave radial Hamiltonian (4). The remaining steps are analogous to the ones leading to equations (13) and (18).

For the calculation of an $n, l \to n', l' = l \pm 1$ interband optical spectrum, in conformity with the selection rule (7*a*), an l-wave radial $E1$ test function is prescribed, analogously to equation (20), as

$$\Psi_l^{(E1)}(r) \equiv \psi_{n,l}^{(h)}(r).$$

$$= \sum_{n'} \left\langle \psi_{n',l'}^{(\mathrm{e})} \left| \frac{1}{r^2} \right| \psi_{n,l}^{(\mathrm{h})} \right\rangle \psi_{n',l'}^{(\mathrm{e})}(r). \tag{28}$$

This test function is then propagated in time with the radial Hamiltonian $V_l^{(\mathrm{e})}(r)$ for $l' = l \pm 1$. The remaining steps are analogous to the ones leading to equation (26).

4. Computational considerations

Accurate solutions of the TDSE

$$i\hbar\frac{\partial}{\partial t}\Psi_l^{(\mathrm{e,h})}(t) = \hat{H}_l^{(\mathrm{e,h})}\Psi_l^{(\mathrm{e,h})}(t) \tag{29}$$

are essential for the successful implementation of the RTWPM. In this work, a simple, but sufficiently accurate, finite-differences technique [8, 18, 19] was employed for the generation of exact numerical solutions on a grid of this equation. The spatial second derivative in the Hamiltonian operator (4*a*) was evaluated by means of a fourth-order five-point formula [18] and the time derivative was evaluated by means of the second-order improved Euler method [8, 18, 19]. Such an integration scheme turns out to be conditionally stable [19]. Fourier transforms were evaluated employing available FFT routines [8].

Due to the boundary condition $\psi_{n,l}^{(\mathrm{e,h})}(r=0)=0$, the wavepacket must satisfy the condition $\Psi_l^{(\mathrm{e,h})}(r=0,t)=0$ at all times, according to equation (27), which can be easily enforced on a grid. On the other hand, since the grid is finite, the artificial condition $\Psi_l(r_{\max},t)=0$ must be imposed, where $r_{\max}$ is the grid boundary. (Another alternative is to impose artificial periodic boundary conditions at $r_{\max}$.) In order to avoid spurious confinement effects, $r_{\max}$ must be chosen large enough so that the calculated bound eigenfunctions decay to zero well before reaching the grid boundary.

Most of the computational effort in the implementation of the RTWPM is spent in the numerical integration of the TDSE. Computation time can be saved, without sacrificing resolution, in the following fashion. From equation (11) it is seen that $A(-t)=A^*(t)$. This implies that $\Omega_T(E)$, equation (12), can be obtained from a time-autocorrelation function constructed for $0\leqslant t\leqslant T$ only, reducing the computation time by half. (In the definition (12) the integral could have been performed for $0\leqslant t\leqslant T$. It can be easily verified that a spectral function defined in this way turns out to be complex, its real and imaginary parts displaying the same information as (13), but with half the resolution. Therefore, it is more convenient to work with the definition (12).) Likewise, according to equation (9), $\Psi(r,-t)=\Psi^*(r,t)$, provided the c_j are real. This implies that, as long as the test function is chosen as real, $\Sigma_T(r,E)$ can also be obtained from a wave function computed for $0\leqslant t\leqslant T$ only.

For a given propagation time, resolution can be further improved by means of standard windowing techniques [8, 20]. This relies on the observation that the Fourier-transform integral of equation (12) can be written with the limits $-\infty\leqslant t\leqslant\infty$ when the integrand is multiplied by the rectangular window function supported on $-T\leqslant t\leqslant T$ [20]. According to the convolution product theorem [20], the finite-resolution spectral function of equation (12) can be regarded as the convolution product of the infinite-resolution spectral function and the lineshape function (15), $\Omega_T(E)=\Omega(E)*\delta_T(E)$. From the computational standpoint, it is more convenient to convolute $\Omega(E)$ with a function whose sidelobes decay faster with energy than those of the lineshape function (15). To this end, the window function

$$\begin{aligned} W_T &= \frac{1}{2}\left(1-\cos\frac{\pi(t-T)}{T}\right) \qquad -T\leqslant t\leqslant T \\ &= 0, t>|T| \end{aligned} \tag{30}$$

was used instead of $P_T(t)$. The modified normalized lineshape function turns out to be

$$\Delta_T(E) = \frac{1}{2}\frac{1}{1-(ET/\pi\hbar)^2}\frac{\sin(ET/\hbar)}{\pi E} \tag{31}$$

$$= L_T(E)\delta_T(E) \tag{32}$$

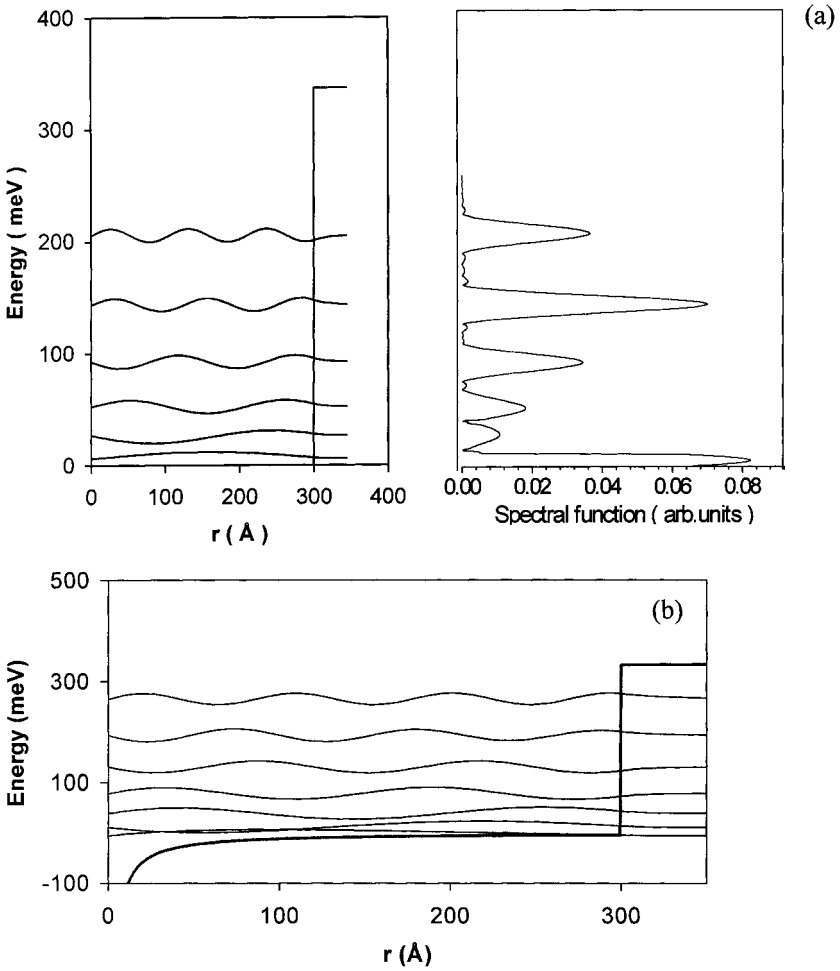

Figure 1. $l = 0$ conduction band radial potential, eigenenergies and eigenfunctions for an $R = 300$ Å GaAs-(Ga,Al)As QD with finite confinement. (a) Without impurity, including the calculated spectral function. (b) With an on-centre shallow donor impurity.

where the definition of the rectangular one is evident and it is seen that its net effect is to strongly damp the sidelobes of $\delta_T(E)$. The same procedure has been employed in the evaluation of the Fourier transforms (17) and (24).

5. Results and discussion

Calculations were performed for GaAs/$Ga_{1-x}Al_xAs$ spherical QD's with a fixed Al concentration of $x = 0.45$. The confinement potential was calculated by means of the empirical formula [15]

$$V_0^{(e,h)} = xA^{(e,h)}(1.247)\ \text{eV} \tag{33}$$

with $A^{(e)} = 0.6$ and $A^{(h)} = 0.4$, yielding $V_0^{(e)} = 336.69$ meV and $V_0^{(h)} = 224.56$ meV. The band gap of pure GaAs is $E_{gap} = 1519$ meV [15]. The spherical effective masses and dielectric constant of GaAs used were $m_e^* = 0.0665m_e$, $m_h^* = 0.30242m_e$ and $\varepsilon_d = 12.35\ \varepsilon_0$ [21].

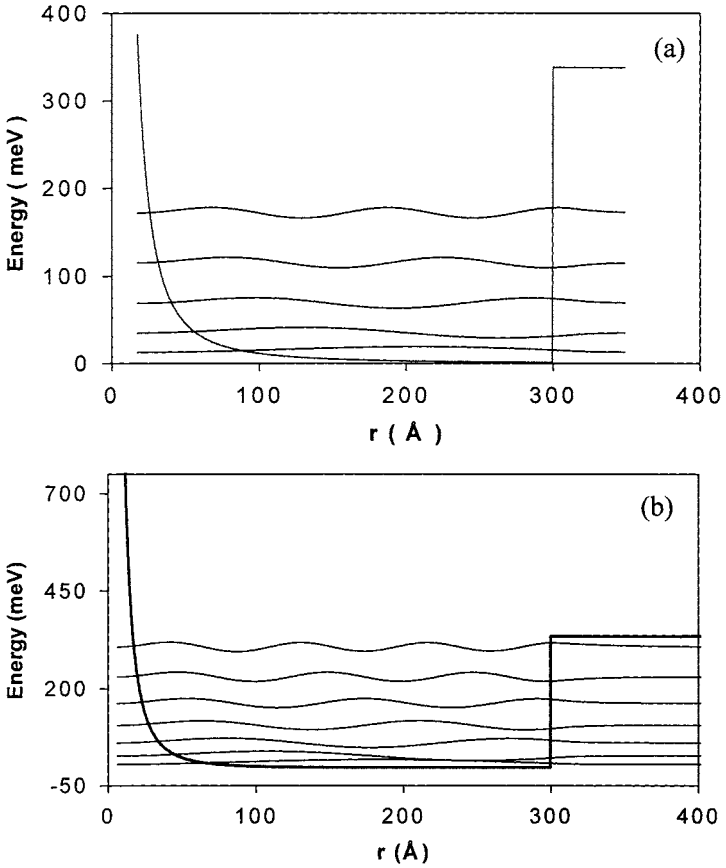

Figure 2. $l = 1$ conduction band radial potential, eigenenergies and eigenfunctions for an $R = 300$ Å GaAs-(Ga,Al)As QD with finite confinement. (a) Without impurity. (b) With an on-centre shallow donor impurity.

Total propagation times ranged from $T = 2.5 \times 10^{-12}$ seconds to $T = 3.75 \times 10^{-12}$ seconds, depending on the level of resolution needed, giving peak breadths of $\Delta E \sim 1.7$ meV and $\Delta E \sim 1.1$ meV, respectively.

Evidently, only the states implicitly comprised in the test function (27) will be displayed in the spectral function and surface of equations (13) and (18), respectively. Therefore, it is desirable to employ a test function that contains as many states as possible. The one function that contains the entire eigenspectrum of the Hamiltonian is the Dirac delta function. However, this function cannot be represented on a discrete mesh. Although there is no general prescription for choosing the best test function, it is expected that a peaked function will overlap with more states than a delocalized one. For the smallest QD's, the entire eigenspectrum was obtained employing a test function with the shape of a narrow Gaussian placed at $r \approx R/2$. For the largest QD's, the entire eigenspectrum was obtained with a test function consisting of two or three Gaussian peaks, distributed more or less evenly within $0 < r < R$.

In order to obtain an $l = 0$ electron or hole energy spectrum, the test function was propagated in time on the corresponding $l = 0$ effective radial potential (4*b*). In order to obtain an $l = 1$ electron energy spectrum *simultaneously* with the $n = 1, l = 0 \rightarrow n', l' = 1$ interband optical spectrum in a single calculation, the hole $n = 1, l = 0$ eigenfunction ($E1$

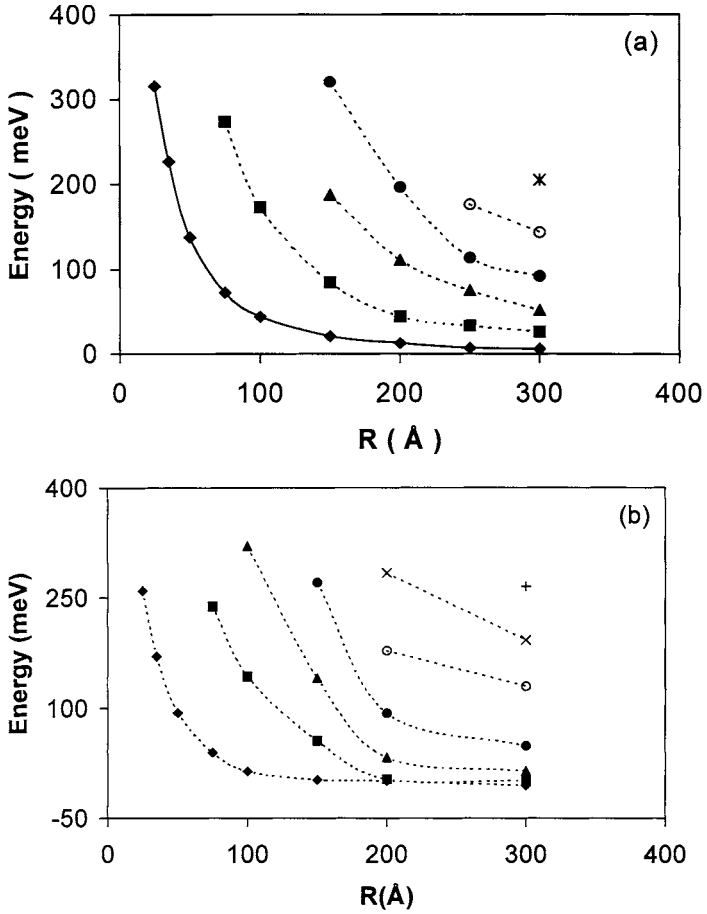

Figure 3. $l = 0$ conduction band eigenenergies for a spherical GaAs-(Ga,Al)As QD with finite confinement, as a function of the radius. (a) Without impurity. (b) With an on-centre shallow donor impurity. ♦, ■, ▲, ●, ○, ×, +, *, –, ◇, □, △, correspond to the ground, first excited, . . . , eleventh excited-state, respectively. The dashed lines connecting the marks are an aid to the eye. The solid line in part (a) represents the analytical ground-state eigenvalues.

test function) was propagated on the conduction-band $l = 1$ potential. The positions and heights of the peaks revealed the $l = 1$ electron energy values and the relative intensities of the corresponding $n = 1, l = 0 \rightarrow n', l' = 1$ interband transitions, respectively.

Figure 1 displays the $l = 0$ conduction band radial potential of an $R = 300$ Å QD, without (a) and with (b) the impurity, together with the entire set of eigenfunctions plotted at the corresponding eigenenergies. Notice that the bottom of the conduction band was assigned the value $E = 0$. Part (a) of this figure also illustrates the corresponding spectral function. This figure was generated by means of a calculation deliberately performed with a relatively low resolution, in order to illustrate the accuracy and efficiency of the method. Indeed, it can be appreciated that the quality of the eigenfunctions obtained is very good, despite the low resolution. It can be seen that the presence of the impurity lowers the energy of the states and gives rise to a new one. Analogous calculations were performed successfully for the valence band (not shown).

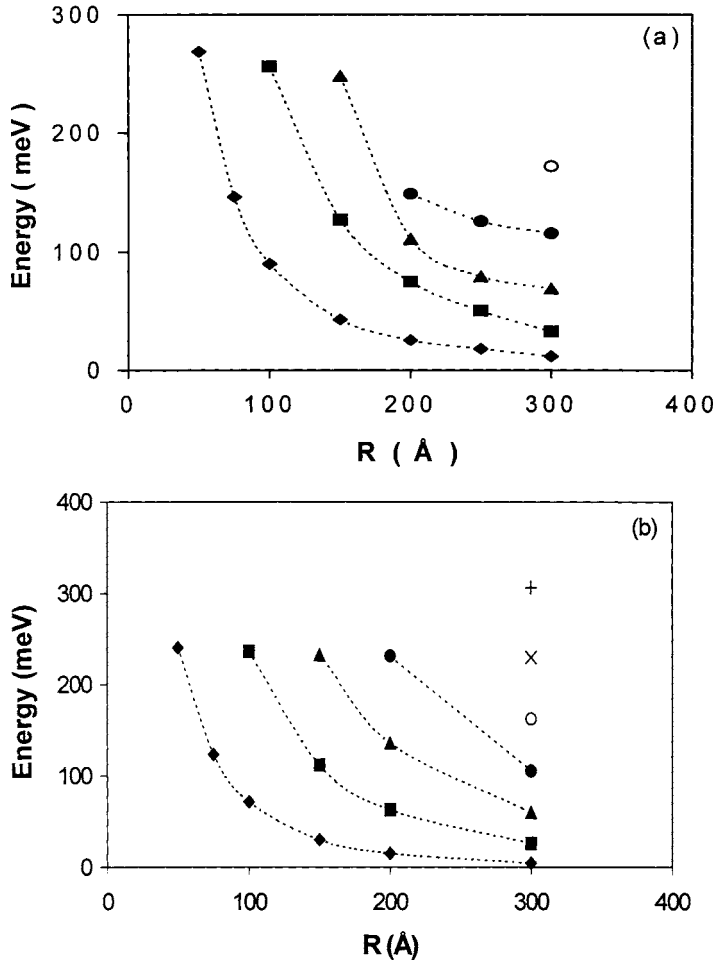

Figure 4. $l = 1$ conduction band eigenenergies for a spherical GaAs-(Ga,Al)As QD with finite confinement. (a) Without impurity. (b) With an on-centre shallow donor impurity. The convention for the symbols is the same as in figure 3.

In figure 2, the $l = 1$ conduction band radial potential of the same QD is depicted, without (a) and with (b) the impurity, with the entire set of eigenfunctions plotted at the corresponding eigenenergies. Notice that, in both situations, the centrifugal term present in the radial Hamiltonian (4*b*) raises the energies of the states in comparison with the $l = 0$ case (figure 1). In fact, without the impurity, it is observed that there is one more state when $l = 0$ than when $l = 1$.

Figure 3 displays the $l = 0$ conduction-band energy eigenvalues without (a) and with (b) the impurity, as functions of the radius of the structure. The marks correspond to the results obtained in this work and the dashed lines connecting them are just an aid to the eye. The solid line in part (a) of this figure represents the ground-state eigenvalues calculated by means of the analytical transcendental equation. Clearly, our numerical results agree excellently with the analytical ones. These plots exhibit the following general features: (i) the ground- and excited-state eigenvalues decrease in an exponential-like fashion with the radius of the QD, the decay being slower the higher the energy. Therefore, there is not a single radius for which bulk

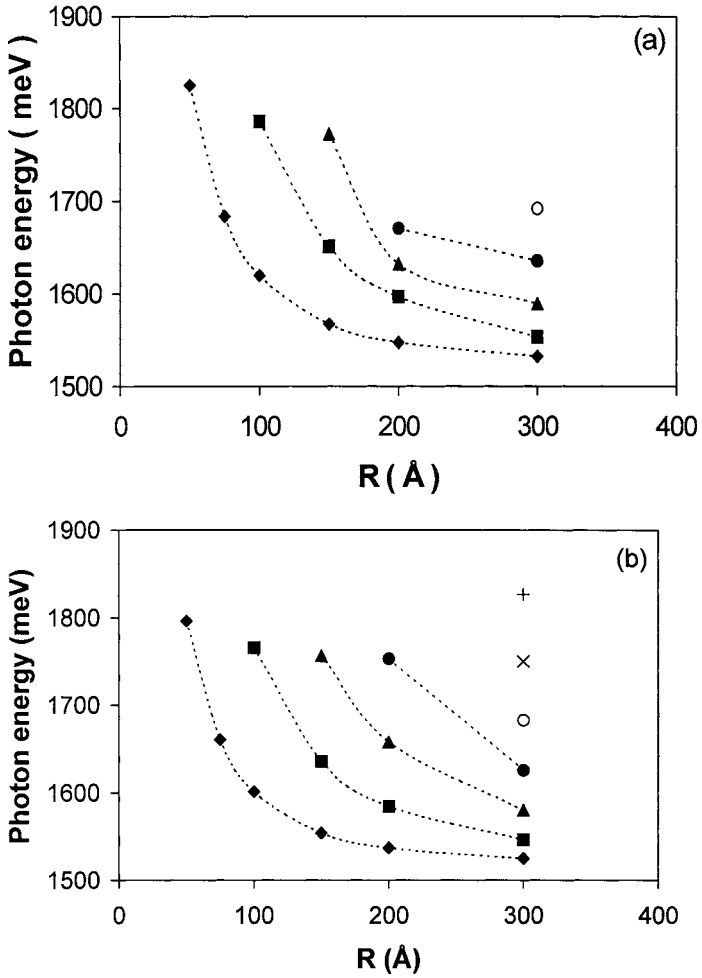

Figure 5. Photon energies of interband transitions in a GaAs-(Ga,Al)As QD with finite confinement, as functions of the radius. (a) Without impurity. (b) With an on-centre shallow donor impurity. ♦, ■, ▲, ●, ○, correspond to the valence band $l = 0$ ground-state → conduction band $l = 1$ ground, first excited, ... fourth excited-state transition energies, respectively. The dashed lines connecting the marks are an aid to the eye.

energy values are attained for different states. (ii) As expected, the number of states supported by the QD increases with the radius. For example, the 35 Å QD supports only one state, while the 75 Å QD supports two. (iii) The presence on the impurity may cause the appearance of new states for a given radius. For example, the 100 Å QD exhibits two states without the impurity and three states with the impurity.

Figure 4 is analogous to figure 3, except that now $l = 1$. The eigenenergies follow the same general behaviour.

Figure 5 shows the calculated photon energies without (a) and with (b) the impurity, as functions of the radius of the structure, for the interband optical spectrum corresponding to the transitions from the $l = 0$ ground state of the valence band to all the $l = 1$ states of the conduction band. It is observed that the photon energy for a given transition decreases in an exponential-like fashion with the radius of the QD.

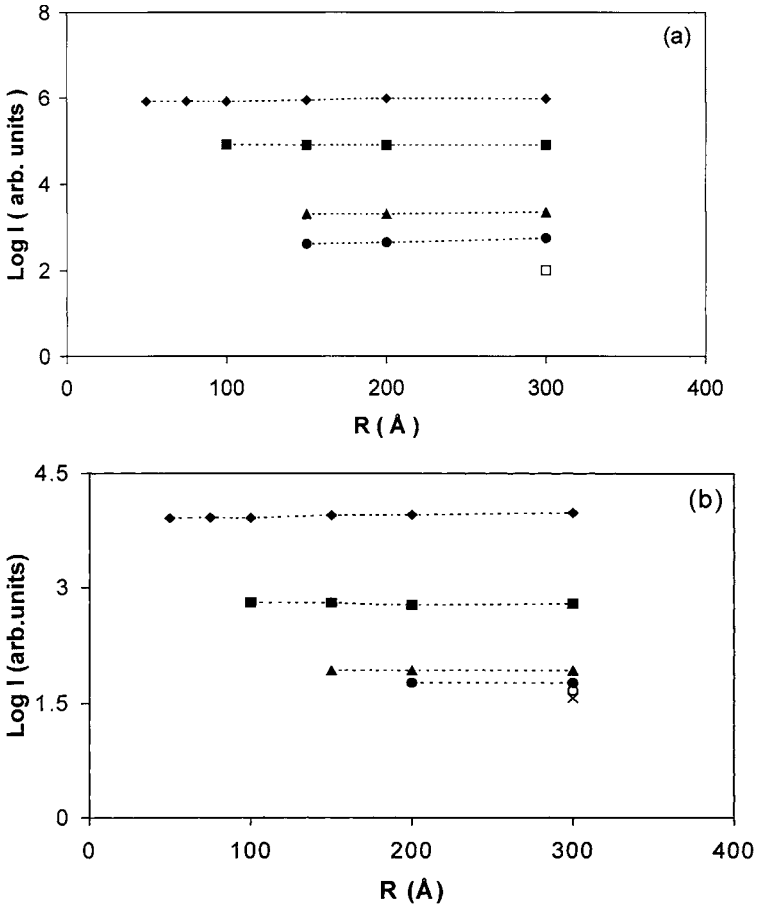

Figure 6. Logarithms of the relative intensities corresponding to the interband transitions of figure 5.

Figure 6 displays the logarithms of the relative strengths corresponding to the interband transitions of figure 5, as given by the second factor of equation (6) and obtained from the test function (28). The following two general features are illustrated by these plots. (i) For a given radius, the intensities decrease very rapidly with the energy of the final state; (ii) the intensities are largely independent of the radius of the QD. The latter result may be particularly useful for the design of optical devices, since it guarantees that a higher-frequency transition can be achieved by decreasing the size of the structure, without any loss in the transition intensity.

In figure 7, the binding energy of the impurity as a function of the radius of the structure calculated by means of the RTWPM is compared with the values obtained by means of the variational approach of reference [15]. It can be seen that the agreement between the two methods is very good. However, our binding-energy results lie slightly higher, which means that our calculated ground-state energies with the impurity present in the structure lie slightly lower. According to the variational principle, this indicates that the RTWPM is more accurate than the variational approach of [15], as it should.

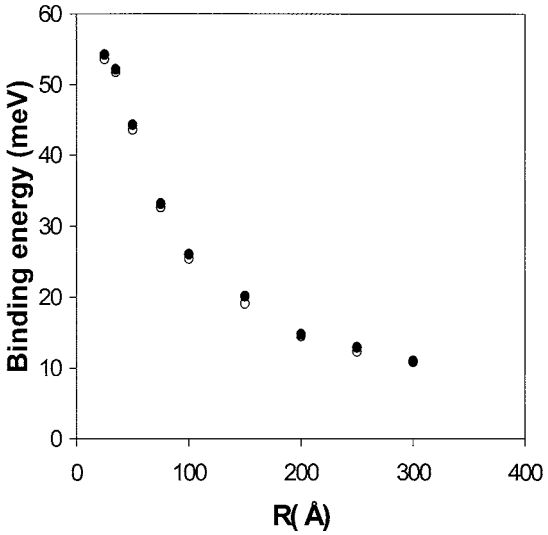

Figure 7. Binding energy of an on-centre shallow donor impurity in a spherical GaAs-(Ga,Al)As QD with finite confinement, calculated by means of the real-time wavepacket propagation method (•) and the variational method of reference [15] (○).

6. Conclusions

We have pointed out a real-time wavepacket propagation methodology for the calculation of discrete eigenenergies, eigenfunctions and optical transition strengths, within the effective mass and single-hole-hand approximations of low-dimensional semiconductor systems. Such methodology was applied to an extensive and systematic study, as a function of the radius, of the entire $l = 0$ and $l = 1$ conduction band quantum states, and the $n = 1, l = 0 \rightarrow n', l' = 1$ interband optical spectra of GaAs-(Ga,Al)As spherical quantum dots with finite confinement, without and with an on-centre shallow donor impurity. The electron–hole interaction was not considered.

The accuracy of the results was seen to be excellent, even for relatively short propagation times. The variety of calculations performed illustrates the versatility and flexibility of the methodology.

For simplicity, in this work the dielectric constant and effective masses were considered equal for the GaAs and (Ga,Al)As materials. Also, the dielectric constant was taken as position-independent and the effective masses as isotropic. These approximations can be easily relaxed in this method, since the values of these variables can be specified at every point on the grid.

The extension of the formalism of the RTWPM to problems involving continuous spectra is straightforward. However, the computational implementation requires special measures, since it is now essential to properly simulate the continuum. An application of the RTWPM to the calculation of Stark shifts, lineshapes, lifetimes and optical transition strengths in quantum wells under strong electric fields will be presented elsewhere.

On the other hand, the extension of this methodology beyond the single-hole-band approximation is a more difficult task, due to the need to deal with matrix Hamiltonians. Research in this direction is currently underway.

We hope that the virtues of this methodology will render it attractive both for experimentalists and theorists interested in the behaviour of the electronic and optical properties of

semiconductor heterostructures as functions of the physical parameters involved in the system.

Acknowledgment

This work was supported in part by Colciencias, under grants 1106-05-421-95 and 1106-05-025-96.

References

[1] Petroff P H, Gossard A C, Logan R A and Wegman W 1982 *Appl. Phys. Lett.* **41** 65
Quinlan S M 1992 *Phys. Rev.* B **45** 9428
Watabe W, Nagamune Y, Sogawa F and Arakawa Y 1996 *Solid State Electron.* **40** 537
[2] Skromme B J, Bhat R, Koza M A, Schwarz S A, Ravi T S and Hwang D M 1990 *Phys. Rev. Lett.* **65** 2050
Jarosik N C, McCombe B D, Shanabrook B V, Comas J, Raltson J and Wicks G 1985 *Phys. Rev. Lett.* **54** 1283
Yoo B S, He L, McCombe B D and Schaff W 1991 *Superlatt. Microstruct.* **8** 297
Yoo B S, McCombe B D and Schaff W 1991 *Phys. Rev.* B **44** 13 152
Salib M S, Nickel H A, Herold G S, Petrou A, McCombe B D, Chen R, Bajaj K K and Schaff W 1996 *Phys. Rev. Lett.* **77** 1135
Itskevich I E, Ihn T, Thornton A, Heinini M, Foster T J, Moriarty P, Nogaret A, Beton P H, Eaves L and Main P C 1996 *Phys. Rev.* B **54** 16 401
[3] Bastard G 1988 *Wave Mechanics Applied to Semiconductor Heterostructures* (Paris: Les Editions de Physique)
Davies J H 1998 *The Physics of Low-Dimensional Semiconductors* (Cambridge: Cambridge University Press)
[4] Bastard G 1981 *Phys. Rev.* B **24** 4714
Altarelli M 1983 *Phys. Rev.* B **28** 842
Greene R L, Krishan K, Bajaj K and Phelps D E 1984 *Phys. Rev.* B **29** 1807
Broido D A and Sham L J 1985 *Phys. Rev.* B **31** 888
Bastard G, Delalande C, Ferreira R and Liu W H 1989 *J. Lumin.* **44** 247
Fraizzoli S and Pasquarello A 1990 *Phys. Rev.* B **42** 5349
Whittaker M 1990 *Phys. Rev.* B **41** 2865
Porras-Montenegro N 1992 *Phys. Rev.* B **46** 9780
Barmby P W, Dunn J L and Bates C A 1994 *J. Phys.: Condens. Matter* **6** 751
Latgé A, Porras-Montenegro N and Oliveira L E 1995 *Phys. Rev.* B **51** 2259
Latgé A, Porras-Montenegro N, de Dios-Leyva M and Oliveira L E 1996 *Phys. Rev.* B **31** 10 160
Latgé A, Porras-Montenegro N, de Dios-Leyva M and Oliveira L E 1997 *J. Appl. Phys.* **81** 6234
[5] Bloss W L 1989 *J. Appl. Phys.* **65** 4789
Lee J, Vassel M O, Koteless E S and Elman B 1989 *Phys. Rev.* B **39** 10 133
Wilson S P and Allsopp D W E 1992 *Superlatt. Microstruc.* **11** 363
[6] Goldoni G and Fasolino A 1995 *Phys. Rev.* B **51** 9903
[7] Winkler R and Rössler U 1993 *Phys. Rev.* B **48** 8918
[8] Potter D 1973 *Computational Physics* (New York: Wiley)
Koonin S E 1986 *Computational Physics* (Reading, MA: Addison-Wesley)
Press W H, Teutolsky S A, Vetterling W T and Flannery B P 1986 *Numerical Recipes* (Cambridge: Cambridge University Press)
[9] Kuhn T, Mahler G, Dunn J L and Bates C A 1994 *J. Phys.: Condens. Matter* **6** 757
[10] Blinder S M 1964 *J. Chem. Phys.* **41** 3412
Rotenberg M 1965 *J. Chem. Phys.* **43** 1657
Blinder S M 1967 *Int. J. Quant. Chem.* **1** 271
Blinder S M 1967 *Int. J. Quant. Chem.* **1** 285
Feit M D, Fleck J A Jr and Steiger A 1982 *J. Comput. Phys.* **47** 412
Feit M D and Fleck J A Jr 1983 *J. Chem. Phys.* **78** 301
[11] Kosloff R 1988 *J. Phys. Chem.* **92** 2087
Kosloff R 1994 *Annu. Rev. Phys. Chem.* **45** 145
[12] Heller E J 1978 *J. Chem. Phys.* **68** 2066
Heller E J 1981 *Acc. Chem. Res.* **14** 368
Hermann M R and Fleck J A Jr 1988 *Phys. Rev.* A **38** 6000
[13] MacKinnon A 1985 *The Recursion Method and its Applications* ed D Weaire (Berlin: Springer)

[14] Gordon R G 1968 *Adv. Mag. Res.* **3** 1
[15] Porras-Montenegro N and Pérez-Merchancano S T 1992 *Phys. Rev.* B **46** 9780
[16] Brandsen B H and Joachain C J 1983 *Physics of Atoms and Molecules* (London: Longmans)
[17] Pérez-Alvarez R and Pajón-Suarez P 1988 *Phys. Status Solidi* B **147** 547
[18] Abramowitz M and Stegun I 1968 *Handbook of Mathematical Functions* (New York: Dover)
[19] Gottlieb D and Orszag S A 1977 *Numerical Analysis of Spectral Methods* (Philadelphia, PA: Society Industrial and Applied Mathematics)
[20] Brigham E O 1974 *The Fast Fourier Transform* (Englewood Cliffs, NJ: Prentice-Hall)
[21] Casey H C Jr 1978 *J. Appl. Phys.* **49** 3684